Real-time *in vivo* confocal fluorescence microscopy

Milind Rajadhyaksha,[1, 2] and Salvador Gonzalez[1]

[1] Department of Dermatology, Harvard Medical School, Wellman Laboratories of Photomedicine, Massachusetts General Hospital, Bartlett Hall Extension 630, Boston, MA 02114

[2] Lucid Inc., 50 Methodist Hill Road, Rochester, NY 14623

1. Introduction

The confocal scanning microscope is well-known for its ability to perform optical sectioning: a thin plane or section within a thick turbid medium is non-invasively imaged with high resolution and contrast [1]. Since its invention and development, confocal scanning microscopes have been extensively used in biomedicine for imaging human and animal tissues *in vivo*. Nuclear, cellular and morphologic detail is imaged in living intact tissue without having to physically excise and prepare thin sections or cultures. By comparison, the conventional microscope images nuclear and cellular detail either within prepared thin sections or in culture (*in vitro*). Histology is a well-known example: it involves the removal of tissue (biopsy), followed by fixing or freezing, cutting into thin sections with a microtome, staining with hematoxylin-and-eosin or other dyes to enhance contrast, and finally, viewing with the microscope.

Real-time confocal microscopes provide a noninvasive window into living tissue for basic and clinical research. Tissue can be imaged in its native state either *in vivo* or freshly excised (*ex vivo*)

without the processing that is necessary for conventional microscopy. Dynamic processes can be noninvasively observed over an extended period of time. For example, the cellular and nuclear morphology of tissue, cell-to-cell interactions, wound healing and tissue regeneration, effects of ultraviolet light, responses to allergic or irritant agents, photoaging, microcirculation, fungal infections, and pharmacokinetics of drug delivery and cosmetics may be directly observed. Among the various types of human and animal tissues, the cornea, retina, skin and oral mucosa are easily accessible and therefore have been most amenable to confocal microscopy. Nuclear, cellular and morphologic detail in epithelial and deeper connective layers, including microcirculation, has been imaged in such tissues with both white-light tandem scanning- and confocal scanning laser- microscopes.

Confocal imaging may be potentially used in the clinic for visualizing lesions and their margins prior to biopsy, diagnosis of lesions without biopsy, or detection of margins either intrasurgically (to guide surgery) or in freshly excised tumors (to guide surgical pathology). Clinical applications include characterization of diseases, including assessment of tumor margins. A related application is rapid morphologic examination in the operating room of surgical specimens, either intra-operatively or freshly excised, without the tissue preparation (fixing or freezing, sectioning, staining) that is necessary for conventional histology.

Confocal imaging may be performed in either reflectance or fluorescence. In reflectance, the contrast arises from native variations in the refractive indices of organelles and microstructures within tissue. Extensive research based on confocal reflectance imaging in both animals and human tissues *in vivo* has been reported in the literature; in particular, a significant effort is currently in progress in dermatology, to study human skin and skin disease. In fluorescence, the contrast is from exogenous fluorophores that are administered to label specific tissue microstructures. (Another source of contrast is autofluorescence – i. e., endogenous or native fluorescence – which is inherently weak but has more

recently been employed by 2-photon confocal microscopy. This is described in the chapter by Peter So et al. in this volume and is not discussed here.) As in reflectance, there has been concomitant research based on confocal fluorescence imaging, especially in small animals. During the past decade, fluorescence studies have been performed on microcirculation in rat brain cortex [2-6], nuclear and cellular morphology in mouse skin [7], rabbit bone [8, 9], rabbit cornea [10], rat bone [11] and rat kidney [12]. Other examples, especially of functional imaging, include those of the epidermis in transgenic mice expressing green fluorescent protein [13], neurons in rat basal forebrain [14], gene expression in rat hippocampus [15], wound repair in rabbit cornea [16], angiogenesis and revascularization in transplanted pancreatic islets [17], and oligonucleotide uptake in skin keratinocytes [18]. Internal organ tissues *in vivo* and surgically exposed tissues *in situ* have also been imaged through excisions with the use of optical fiber-based confocal microscopes in endoscope-configurations; tissues include colon and vas deferens [19-22] and peritoneum [23, 24]. Human studies include evaluation of microvascular patterns in choroidal melanomas [25], and largely unpublished work on skin morphology by various industry research groups. The morphology and function in plants *in vivo* has also been of interest [26-29]. Typically, the fluorophore has been administered either topically or by intravenous injection.

Compared to reflectance, the contrast produced by fluorescence can be much more sensitive and specific to tissue microstructure and function. Both the significant number of publications during the last few years as well as recent development of commercial confocal fluorescence microscopes specifically for *in vivo* use clearly indicate the growing interest in fluorescence contrast. However, the full potential of fluorescence-based imaging for both animal and human applications is yet to be realized, probably because real-time confocal detection of fluorophores within tissue *in vivo* is challenging. Delivery of fluorophore molecules at a specific site followed by clearance of unbound

molecules is not easy. Moreover, fluorescence emission is subject to fundamental limitations due to photobleaching or excited singlet (or triplet) state saturation, such that, at low, non-toxic fluorophore concentrations, the signals may be weak. One, thus, requires a careful understanding of the physics of fluorescence with detailed attention to the optimization of instrumentation design and imaging parameters. Brakenhoff and Visscher [30] provide an excellent introduction to this topic. Factors governing successful real-time imaging *in vivo* include choice of fluorophore and its photophysics, and confocal microscope design parameters such as choice of optics and objective lenses, scanning configuration, resolution, collection and transmission efficiency, frame rate or detector integration (pixel) time, chromatic aberrations within the optics, spherical aberrations within the tissue, scattering and absorbing properties of the tissue, and opto-electro-mechanical methods to stabilize tissue. With effort toward understanding and applying these factors, the full potential of confocal fluorescence imaging can be realized. In this chapter, we will quantitatively look at the possibilities (and limitations) and applications of real-time confocal fluorescence microscopy for basic research and clinical applications in animal and human tissues *in vivo*. The results of our analytical and experimental studies as well as those of other groups are presented, including a review of the literature.

2. Concepts of confocal imaging

Over the last four decades since its invention, the theory and practice of the confocal microscope have been well established [31-34]. In this section, we provide a brief introduction to the main concepts of confocal imaging, and list the original references that contain the detailed theory.

2.1 Optical sectioning

A confocal microscope is made up of a small, bright source of light that illuminates a small three-dimensional spot within the object (figure 1). The illuminated spot is imaged onto a detector through a small aperture (pinhole). The source of light, illuminated spot and detector aperture lie in optically conjugate focal planes, and hence this configuration is called "confocal." Because we illuminate only a single small spot at a time and image through a small aperture, the detector receives light only from the single illuminated spot that is in focus. Light from all other spots that are either axially or laterally away from focus is rejected (or spatially filtered) by the small aperture in front of the detector. The spot may be scanned in two dimensions to illuminate and image a plane. Thus, with a confocal microscope, we image the single specific plane that is in focus within the object. Thin slices or sections are non-invasively imaged; this is called optical sectioning. Illuminating with a small spot and imaging through a small detector aperture provides high axial resolution and high contrast (i. e., strong rejection of light from all out-of-focus planes that, otherwise, would cause blur).

By comparison, a conventional microscope consists of a large source of light that illuminates a large spot (large volume) within the object, that is then imaged onto a detector through a large aperture. (When you directly view the object, the pupil in your eye is the large aperture.) The detector receives light from the plane that is in focus as well as planes that are away from focus. Conventional microscopes therefore do not have axial resolution and lack optical sectioning capability (figure 2). Consequently, the object has to be physically cut into thin sections and stained before viewing.

It is obvious from figure 1 that the confocal microscope is essentially a point illumination and point detection system. Information about a single spot within an object is useful in many situations, but often, we want an image of a large portion of the object. To create an image, the illuminated spot is

scanned over the desired field of view: we illuminate the desired area of interest on the object point-by-point in a two-dimensional matrix (raster) and then build up the image correspondingly point-by-point. Scanning is accomplished either by keeping the illuminated spot stationary and moving the object (known as object scanning) or by moving the illumination beam over the stationary object (known as beam scanning). Although figure 1(a) shows light to transmit through the object, the illumination light will actually not penetrate through an animal or human being. Hence, we detect back-scattered light, with the illumination and detection being on the same side of the object (figure 1b).

Object scanning has several advantages. The optical system is simple, and because the beam is stationary and always on-axis, we obtain diffraction-limited resolution and constant illumination across the entire object. The object can be moved to obtain as large a large field-of-view as necessary, independently of the objective lens specifications; thus, a large field-of-view is possible with a high magnification, high numerical aperture (NA) lens. High NAs are often required for adequate axial resolution (confocal sectioning), particularly to visualize nuclear and cellular detail. A high NA collects more of the fluorescent light and improves detection sensitivity. Moving an object by electro-mechanical means is slow, which provides longer detection times and, again, higher detection sensitivity. These powerful advantages, unfortunately, lead to one significant limitation: object scanning cannot be used for imaging animals or humans *in vivo*. With the recent advent of optical and non-optical imaging modalities, *in vivo* imaging has rapidly gained importance for basic and clinical research in biomedicine. Real-time imaging of animal or human tissue *in vivo* requires fast beam scanning. Here, the optics is complex and lossy. Because the beam is scanned, off-axis aberrations and vignetting causes both the resolution and illumination to vary across the field-of-view. The scan angles and objective lens magnification define the field-of-view; thus, high NA lenses with their

correspondingly high magnifications result in rather small, limited fields-of-view. Fast scanning also results in short detection times and hence lower detection sensitivity. The message here, rather obviously, is that real-time confocal fluorescence imaging *in vivo* is challenging.

2.2 Reflectance point spread function

The impulse response (i. e., the three-dimensional image of a point object) of a conventional microscope is mainly defined by the three-dimensional point spread function (PSF) of the objective lens that performs the imaging. In general, the condenser lens is used mainly to illuminate the object with a large source of light; since this lens is not involved with imaging the object, it makes a minor contribution to the resolution. The PSF of the objective lens with a clear, circular aperture is well known to be the Airy function in the lateral plane (this is the plane perpendicular to the optical axis) and a sinc^2 function in the axial plane (plane containing the optical axis) [35, 36]:

$$\text{Lateral: } I_{conv}(v) = [2\, J_1(v) / v]^2 \qquad (1)$$

$$\text{Axial: } I_{conv}(u) = [\sin(u/4) / (u/4)]^2 \qquad (2)$$

where I denotes irradiance and J_1 is the well-known first order Bessel function of the first kind. For a given objective lens, with numerical aperture $NA = \sin\alpha$, the optical units v and u relate to the physical coordinates r (radial distance from the optical axis) and z (axial distance from the focus) according to $v = (2\pi/\lambda)\, r \sin\alpha$ and $u = (8\pi/\lambda)\, z \sin^2(\alpha/2)$. [This, of course, assumes that the objective lens images through air. If the lens images through an immersion medium of refractive index n, such that $NA = n \sin\alpha$, then $v = (2\pi/\lambda)\, r\, n \sin\alpha$ and $u = (8\pi/\lambda)\, z\, n \sin^2(\alpha/2)$.]

In a confocal microscope (figure 1), both the condenser lens and the objective lens perform imaging, and therefore the impulse response is defined by the product of the PSFs of the two lenses [31, 32, 34, 37-40]:

Confocal PSF = Condenser lens PSF x Objective lens PSF

= Illumination PSF x Imaging PSF (3)

Imaging tissue *in vivo* using the epi- or back-scattered configuration (figure 1b) means that we illuminate and image through the same lens: the condenser lens is the same as the objective lens ($NA_{condenser} = NA_{objective} \equiv NA$). When we use a confocal microscope to look at a point object in reflectance, using either monochromatic or colored light, the imaging is at the same wavelength(s) as the illumination ($\lambda_{illumination} = \lambda_{imaging} \equiv \lambda$), such that the confocal PSF is

Reflectance, lateral: $I_{conf}(v) = [2\ J_1(v) / v]^4$ (4)

Reflectance, axial: $I_{conf}(u) = [\sin(u/4) / (u/4)]^4$ (5)

assuming, again, clear, circular apertures for both lenses. The full width at half maximum of these PSFs defines the confocal resolution. Assuming incoherent, uniform illumination, the resolution of a confocal microscope is thus

Reflectance, lateral: $\Delta x = 0.46\lambda/NA$ (6)

Reflectance, axial: $\Delta z = 1.4n\lambda/NA^2$. (7)

The factors 0.46 and 1.4 vary depending on the illumination being incoherent or coherent, and planar or spherical wave (uniform or Gaussian irradiance). The axial resolution in equation (7) defines the diffraction-limited thickness of the optical section that is imaged by the confocal microscope. For pinholes of diameter larger than ~20 optical units (i. e., v > 10), a purely geometrical optics perspective gives a reasonable estimate of the section thickness. Here, the section thickness may be determined from the detected signal drop-off as a function of distance z from the focal plane [41, 42]. The detected signal drops off as

$$C(z) = 1 / [1 + (z/d_p)\, M \tan \alpha]^2 \quad (8)$$

where d_p is the detector aperture (pinhole) diameter, M is the magnification and α is the half-angle of the light cone defined by the NA. The full width at half maximum of C(z) gives us the geometrically defined section thickness to be [42, 43]

$$\Delta z_{geometrical} \approx \sqrt{2}\, d_p / (M \tan \alpha) \quad . \quad (9)$$

2.3 Fluorescence point spread function

In fluorescence, the (incoherent) impulse response is very different, because the imaging (i. e., fluorescence emission) wavelength is not the same as the illumination (i. e., excitation) wavelength [41, 42, 44-52]. In fact, the imaging wavelength is longer than the illumination wavelength by the

Stokes shift ($\lambda_{imaging} > \lambda_{illumination}$). The lateral and axial PSFs now depend on the ratio $\beta = \lambda_{imaging} / \lambda_{illumination}$ [32, 46]. The confocal PSF, for a point object, is now

Fluorescence, lateral: $I_{conf}(v) = [2 J_1(v) / v]^2 [2 J_1(v/\beta) / (v/\beta)]^2$ (10)

Fluorescence, axial: $I_{conf}(u) = [\sin(u/4) / (u/4)]^2 [\sin(u/4\beta) / (u/4\beta)]^2$ (11)

The optimum resolution is obtained when $\beta \rightarrow 1$, meaning that the fluorescence imaging wavelength should be close to the illumination wavelength. Equations (10) and (11), of course, assume the simple case of illumination and imaging at single wavelengths through narrow band-pass filters. Often, in reality, we may use a range of wavelengths with either short-pass or long-pass filters. This is especially true for real-time *in vivo* imaging where the detected fluorescence signal from a fluorophore at a low, non-toxic concentration, deep within tissue may be weak, necessitating broad-band detection. Detecting a range of wavelengths increases the section thickness. In other words, the axial resolution (section thickness) is proportional to β, and if β becomes very large ($\beta \rightarrow \infty$), the sectioning degrades and the imaging becomes similar to that of an incoherent conventional microscope.

Equations (10 and (11) assume the ideal condition of a point detector aperture (i. e., pinhole diameter is equal to the diffraction-limited lateral resolution). Since, in reality, the fluorescence may often be weak, one may have to increase pinhole diameter to increase signal-to-noise ratio while accepting an increase in section thickness [46, 53-55]. The sectioning remains constant over a range of small pinhole diameters that are close to the diffraction limit, but then degrades (somewhat linearly) as the pinhole diameter further increases; that range becomes small as β increases, however. With large pinholes, the sectioning can be defined on the basis of geometrical optics, as in equations (8) and (9)

[41, 42]. Here, the inverse square-dependence of the detected signal on the sectioning implies that the total detected signal drops as 1/t for out-of-focus layers of thickness t. This effect suppresses the background fluorescence.

The above discussion is only a summary of the main concepts of confocal imaging. The detailed theory is well explained in the original references that were mentioned. Our main concern here, from an applications perspective, is detectability of signal to better understand the possibilities and limitations of fluorescence imaging in animals and humans. Indeed, detectability has been previously proposed as a criterion for the design and evaluation of confocal microscope performance [56, 57].

3. Detectability of fluorescence signal

Real-time high-resolution confocal fluorescence imaging in tissue *in vivo* is challenging. At fluorophore concentration that is low enough to be non-toxic to the tissue, the very small illuminated confocal spot may not contain enough fluorophore molecules to produce a strong fluorescence signal. Moreover, in real-time, the detector may not have a sufficiently long integration time for each pixel to collect a sufficiently large number of fluorescent photons. For example, for a typically high NA of 0.9 (water immersion) and illumination wavelength λ of 488 nm, the diffraction-limited resolution is ~0.3 μm (lateral) and ~1 μm (axial or section thickness) and thus the imaged confocal spot is ~10^{-13} ml. At a typical dosage of ~1 μMolar, we might expect ~60 molecules in the confocal spot, and at a typical fluorescence emission rate of ~10^{8} photons per molecule-second, with a detector integration time of ~100 nsec (video-rate), each pixel in the image would collect ~600 photons. Underlying this signal may be a background noise of ~200 photons, and therefore the quantum-limited signal-to-noise ratio [i.

e., √(signal+background)] would be ~28, and contrast (i. e., signal/background) ~3. Fortunately, the picture (or image!) is not as gloomy as it looks at first glance. Our experimental experience has taught us that it is possible, by using reasonably good-yield fluorophores and with careful optimization of microscope optics, to confocally image tissue *in vivo* at high resolution and in real-time.

3.1 Singlet state-excitation

Any experiment must necessarily begin by estimating the detected signal (number of detected fluorescent photons) for our chosen fluorophore and imaging conditions, so that we understand our chances of success. We expect the detected number (S) of fluorescent photons in a pixel in the image to be:

$$S = F\ N\ f_{lens}\ T_{tissue}\ T_{optics}\ t_{detector} \tag{12}$$

where

F = Fluorescence emission rate [photons per fluorophore molecule per second],

N = Number of fluorophore molecules in the imaged confocal spot,

f_{lens} = fraction of the fluorescence emission that is collected by the objective lens,

T_{tissue} = fraction transmitted by tissue,

T_{optics} = fraction transmitted by the confocal microscope optics,

$t_{detector}$ = detector integration time (pixel time) [seconds].

For a fluorophore with an emission quantum efficiency η, absorbance or excitation rate k_a [photons/molecule second] and decay or emission rate k_f [photons/molecule second], the fraction of molecules that are in the excited state is given by the ratio $k_a / (k_a + k_f)$. This assumes excitation from the ground state to the lowest singlet state, with the excited singlet state lifetime being τ_f. Note that $\tau_f = 1/k_f$. (The triplet state is considered later.) Then, the fluorescence emission rate [photons/molecule second] is [58, 59]

$$F = \eta \, k_f \, k_a / (k_a + k_f). \tag{13}$$

One can calculate the absorbance or excitation rate [photons/molecule second] as

$$k_a = \sigma \, I / h\nu \tag{14}$$

where σ [cm^2 /molecule] is the absorbing cross-section, I [Watts/cm^2] is the irradiance, and $h\nu$ [Joules/photon] is the energy of a photon. (Planck's constant, $h = 6.626 \times 10^{-34}$ Joule-second, frequency of the illumination, $\nu = c/\lambda$, with speed of light $c = 3 \times 10^8$ m/second and λ being the wavelength.) For the excited singlet state condition, the maximum signal-to-noise ratio is obtained under steady state, when the excitation rate k_a is equal to the emission rate k_f. This condition, $k_a = k_f$, then defines the optimum illumination irradiance to be

$$I_{optimum} \, [\text{Watts/cm}^2] = k_f \, h\nu / \sigma \; . \tag{15}$$

When the actual illumination irradiance I is less than the optimum (i. e., $I < I_{optimum}$), the fluorescence emission rate is proportional to I such that the detected signal increases with increased illumination

irradiance. When the illumination irradiance exceeds the optimum (i. e., $I > I_{optimum}$), however, the excited states saturate; with almost all molecules now in the excited state and almost none in the ground state, increasing I does not further increase the signal but causes the background noise to linearly increase. This background noise originates due to fluorophore molecules or autofluorescence from out-of-focus (i. e., outside the imaged confocal spot) regions of the tissue. Outside the confocal spot, the fluorophore molecules are still in their ground state and continue to fluoresce since the illumination irradiance there is still less than the optimum.

3.2 Triplet state-excitation

When a fluorophore has a high quantum efficiency for transition from singlet to triplet state (intersystem crossing), a large fraction of the illuminated molecules will be trapped in a long-lived triplet state, and consequently, the fluorescence emission decreases. If η_{ISC} is the intersystem crossing efficiency and τ_T is the triplet state lifetime, then the triplet state will fill up at a rate k_T [58, 59]:

$$k_T = 1/\tau_T + \eta_{ISC}\, k_f\ \ k_a / (k_a + k_f). \tag{16}$$

In other words, the triplet state fills up in time constant $1/k_T$. In this situation, the fluorescence emission rate is

$$F = \eta\, k_a / [1 + k_a\, (1/k_f + \eta_{ISC}\, \tau_T)]. \tag{17}$$

The decrease in fluorescence emission, according to equation (17), will happen if the dwell time (i. e., illumination time) per spot exceeds the triplet state lifetime.

3.3 Photobleaching

Photobleaching occurs when the triplet state in the fluorophore reacts with molecular oxygen, forming a non-fluorescing molecule. Fluorophore molecules will photobleach with a quantum efficiency η_b and at a rate k_b [58, 59]:

$$k_b = \eta_b \, k_f \, k_a / (k_a + k_f). \tag{18}$$

This gives the time constant of photobleaching as $\tau_b = 1/k_b$ which is the time after irradiation when only 37% (e^{-1}) molecules remain. (According to Sandison et al. [59], photobleaching tends to limit the fluorescence emission to a maximum of $\sim 10^5$ photons/molecule-second for some of the best fluorophores in living cells.)

3.4 Steady-state maximum signal

From equation (14), the optimal irradiance I [Watts/cm^2] is

$$I = k_a \, h\nu / \sigma \tag{19}$$

where k_a now depends on whether the excited fluorophore molecules are in the singlet or triplet state. For fast scanning such that the dwell time (i. e., illumination time) at each pixel is shorter than the time required for triplet state fill-up, the maximum signal is obtained under steady state condition, when the excitation rate equals the emission rate: $k_a = k_f = 1/\tau_f$. For slow scanning (long dwell times) that allows the triplet state to fill up, the steady state maximum signal is obtained when $k_a = 1/(\tau_f + \eta_{ISC} \, \tau_T)$.

4. Performance of a prototype video-rate confocal microscope

We built a video-rate confocal scanning laser microscope for imaging skin and other tissues *in vivo* [60-62]. The microscope was originally designed for reflectance, but we modified and used it for fluorescence imaging of the stratum corneum in human skin and the epidermis and dermal microcirculation in small animals. These experiments were performed to investigate feasibility and the results provide insight into the possibilities (and limitations) of real-time confocal fluorescence imaging in tissue *in vivo*. Calculated or experimentally measured values for the instrumentation parameters (N, f_{lens}, T_{tissue}, T_{optics}, $t_{detector}$) of equation (12) are shown.

4.1 Volume of the imaged confocal spot

High-resolution, high-contrast imaging within living tissue demands water immersion objective lenses with high numerical aperture (NA). To visualize nuclear and cellular detail in tissue and blood circulation, the NA must be higher than 0.7 [61]. We usually use NA of 0.9. The imaged spot, defined by the focused cone of light that is within the confocal section (figure 3a), is of volume

$$V = (\pi/12)\,[(\Delta z)^3 \tan^2\theta + 6\,(\Delta x)(\Delta z)^2 \tan\theta + 12\,(\Delta x)^2(\Delta z)] \qquad (20)$$

where Δx is the lateral resolution and Δz is the section thickness (axial resolution) and θ is the half-angle of the focussed cone ($NA = n\sin\theta$ for immersion medium of refractive index n). Under ideal, diffraction-limited conditions, Δx and Δz are defined by equations (6) and (7). With blue illumination

at 488 nm and a water immersion (n=1.33) objective lens of NA 0.9, the calculated diffraction-limited lateral resolution is 0.3 μm and section thickness is 1.1 μm. In reality, however, the section thickness depends on the detector aperture (pinhole) size [53], chromatic aberrations due to the optics [59, 63, 64] and spherical aberrations that occur when imaging deep within tissue [65, 66]; at high NAs, the sectioning degrades by a factor of about two from the diffraction limit when imaging in skin [61, 64, 67]. We experimentally measured the lateral resolution (Δx) to be 0.5 μm and section thickness (Δz) to be 2 μm at a depth of ~100 μm within living human skin when using a pinhole diameter of 10 resels. (i. e., v = 15 optical units. One resel is equivalent to the lateral resolution Δx [34], and based on equation (6), v = 1.5 optical units when the pinhole diameter is equal to one resel). Then, the imaged spot volume V is 6×10^{-12} ml.

4.2 Number of fluorophore molecules

The number (N) of fluorophore molecules in the imaged confocal spot is easily determined from the dosage (milligrams of fluorophore per kilogram of body weight), known blood volume (milliliters per kilogram of body weight), and the fact that one mole is equivalent to the molecular weight in grams and contains Avogadro's number (6×10^{23}) of molecules:

$$N = \{\text{dosage [mg/kg]} / \text{blood volume [ml/kg]}\}\ \{\text{imaged spot volume V [ml]}\}\ \{6 \times 10^{23}\ \text{[molecules/mole]} / \text{molecular weight [gm/mole]}\}\ \{10^{-3}\ \text{[gm/mg]}\} \quad (21)$$

4.3 Fluorescence light collected by objective lens

Assuming that the fluorescence emission is uniformly distributed in a spherical volume of 4π steradians about the illuminated spot (figure 3a), the objective lens will collect fluorescent photons within the solid angle defined by the NA (NA = $n\sin\theta$). That solid angle is $2\pi(1-\cos\theta)$, and thus the fraction of the fluorescence emission that is collected by the objective lens is

$$f_{lens} = (½)\,(1-\cos\theta). \quad (22)$$

For our water immersion (n=1.33), 0.9 NA lens, the fraction turns out to be 13%.

4.4 Fluorescence light transmission through living tissue

The fluorescent photons collected by the objective lens must migrate first through the tissue and then through the microscope optics before reaching the detector. Visser et al. [68] report a detailed analytical model to account for and correct for loss of both excitation and fluorescence light in a turbid medium, for reconstructing three-dimensional stacks of confocal images. Based on analytical results from a finite-difference time-domain model [69, 70] as well as our experimental data in human skin samples, we expect an exponential (Beer's law) loss of photons in the epidermis and dermis, such that the fraction of fluorescent light transmitted by tissue is

$$T_{tissue} = e^{-\mu t\, z} \quad (23)$$

with μ_t being the net extinction coefficient due to scattering and absorption, and z the depth of imaging. The values for μ_t reported in the literature widely vary, and hence we choose representative estimates: $\mu_t = 10\ mm^{-1}$ for human epidermis and $\mu_t = 25\ mm^{-1}$ for human dermis at the blue wavelength 488 nm [71]. In the absence of data for small animal tissues, we will use the same values

for animal skin. Assuming illumination at 488 nm (which is the wavelength that we have most used), the measured maximum depth of imaging in ~100 μm. This includes microcirculation in the dermis that typically occurs between 50-100 μm deep. Given these parameters, the fraction (T_{tissue}) of fluorescent light transmitted by tissue is estimated to be 60%-37% from a depth of 50-100 μm in the epidermis and 8% from a depth of 100 μm in the dermis.

4.5 Fluorescence light transmission and detection by the confocal microscope optics

Beyond the tissue, the fraction (T_{optics}) transmitted by the microscope optics was measured to be 50%. (The transmission of 50% is actually poorer than normal, mainly because our microscope is optimized for reflectance and longer near-infrared wavelengths, and moreover, the optics in the original prototype was not of the best quality. A well-designed well-optimized microscope will generally provide 65-80% transmission, as we have determined in a recent, new setup.) Finally, the fluorescent photons are detected over an integration time ($t_{detector}$) of 100 nsec/pixel when the imaging is at video-rate (30 frames/sec). The above analysis, from equation (12) to (23), addresses the question of detectability: how many photons per pixel will we detect? This analysis is, of course, somewhat approximate. Also available is a more rigorous Monte Carlo simulation of detected fluorescence in a turbid medium [72]. Although approximate, the analysis has nevertheless proven to be quite useful for predicting detectability, as demonstrated by the experimental results shown below.

4.6 Quantum- and background- noise

Within the detected signal (S), there is quantum noise that varies as the square root of S (i. e, quantum noise = $\sqrt{S}$). Moreover, underlying the detected signal will be background noise (B) due to

fluorophore molecules that are outside the confocal section, tissue endogenous autofluorescence, Raman fluorescence, and backscattered (reflected) light that may leak through inefficient filters. The detected signal-to-background ratio (S/B) determines the contrast in an image, and the signal-to-noise ratio ($S/\sqrt{S}$) determines its useful information content or image quality [59, 73-75]. Gan and Sheppard [56] and Sheppard et al. [57] have presented a thorough analysis of detectability in terms of signal-to-noise ratio, taking into consideration all sources of noise from quantum effects, optical instrumentation and object background. In fact, they propose detectability to be a rigorous measure of confocal microscope performance. Furthermore, in practical applications involving non-ideal objects such as living tissues, the image contrast and signal-to-noise ratio may also limit the obtainable resolution (i. e., the resolution will likely not be diffraction-limited as defined by equations (6) and (7)) [34, 76]. When the detected signals are low, as may happen from small object features, the resulting contrast may not be adequate to distinguish between closely spaced object features, leading to a loss of resolution.

5. Detectability of common fluorophores: analytical and experimental examples

Commonly used fluorophores are listed in Tsien and Waggoner [58] and Terasaki and Dailey [77], and Cullander [78] provides excellent practical advice on their usage for confocal imaging. (See, also, the references in all these book chapters.) Several general references that list fluorophores and their properties are available [79-86]. The emission quantum yield η of fluorophores strongly depends on the micro-environment, and thus is often not known within tissues or blood. The best we can do is to assume the quantum yield of fluorophores in their solvents. Such calculations, nevertheless, provide an initial estimate of signal level – and indeed whether one might expect a signal at all! We have

found it useful to validate the math with calibrated experiments on excised tissue (*ex vivo*) or *in vitro* specimens; this helps to estimate the range of optimum instrumentation and imaging parameters for the subsequent *in vivo* experiments.

Our experiments in confocal fluorescence have mostly been to image microvasculature and blood flow in small rats (weight ~300 mg, blood volume ~70 ml/kg) using a fluorophore dosage of ~1mg/kg, with a 60X, 0.9 NA water immersion objective lens, blue illumination wavelength of 488 nm, and a pinhole diameter of 1 mm (i. e., 10 resels for which v=15 optical units). The confocal spot volume is estimated to be $6x10^{-12}$ milliliters. For the calculations, we assume imaging of microcirculation in the dermis at a depth of 100 μm, from which the fraction (T_{tissue}) of fluorescent light transmitted by tissue is 8%. The fraction (T_{optics}) transmitted by our confocal microscope optics is 50% and the detector integration time ($t_{detector}$) at video-rate is 100 nsec/pixel.

5.1 Fluorescein in aqueous solution

Fluorescein (molecular weight 376) in aqueous solution has the following properties: emission rate k_f = $2.2x10^8$ photons/molecule-second, molar extinction coefficient ε = 80000 liters/Mole-cm that is equivalent to an absorbing cross-section $\sigma = 3x10^{-16}$ cm^2/molecule [$\sigma = (\ln 10)\varepsilon$], excited singlet state lifetime τ_f = 4.5 nsec, quantum yield η = 0.9, intersystem crossing efficiency η_{ISC} = 0.03, triplet state lifetime τ_T = 1000 nsec, peak excitation wavelength λ_{ex} = 490 nm and peak emission wavelength λ_{em} = 515-520 nm.

We have $1.4x10^5$ molecules in the imaged confocal spot volume. For the excited singlet state condition, the maximum signal-to-noise ratio is obtained under steady state when the excitation rate k_a

is equal to the emission rate k_f. The math, using equations (13) to (23), then tells us to expect the detected signal to be 7200 photons/pixel or 28 nW. (At 488 nm and video-rate pixel integration time of 100 nsec, 1000 photons is equivalent to 4 nW.) This detected fluorescence signal compares well to that detected in reflectance; when imaging skin in reflectance with 1 milliwatt illumination at 1064 nm, we typically collect 1000-10000 photons/pixel (i. e., 10-100 nW) relative to a background of 100-500 photons/pixel [61]. Figure 4 shows fluorescein-labelled microspheres in rat microcirculation; this demonstrates the (rather well-known) detectability of fluorescein within blood flow.

The triplet state will fill up at a rate $k_T = 4.3 \times 10^{-6}$ per second, which means that the triplet state fills up in 232 nsec. At video-rates, the pixel time is 100 nsec, and thus one tends to ignore the partial fill-up of the triplet state. However, at slower frame rates, one cannot ignore the eventual triplet state fill-up that will reduce the fluorescence emission. In this situation, the maximum signal-to-noise ratio is obtained when $k_a = 1/[\tau_f + \eta_{ISC}\, \tau_T]$. Using equation (17), we now find the detected signal to be 950 photons/pixel. This represents an almost eight-fold drop in signal which, to some extent, can be compensated for with the slower frame rate (i. e., longer pixel time or detector integration time). Given that the triplet state lasts for 1000 nsec, longer detection time will certainly help.

Fluorescein has a photobleaching quantum efficiency (η_b) of 3×10^{-5} which means that the photobleaching time is 300 μsec. Since this is much longer than the dwell time (i..e., illumination time) per pixel of 100 nsec for video-rate scanning, photobleaching does not occur. The optimum irradiance for maximum signal is then calculated to be 3×10^5 Watts/cm^2 within the microvasculature which, over a diffraction-limited spot diameter of 0.65 μm (for blue 488 nm Argon-ion laser wavelength 488 nm, water immersion 0.9 NA objective lens), corresponds to 1 milliwatt of illumination power. Assuming the blood vessels to be 100 μm deep in the dermis, which is the

maximum depth that can be seen with a video-rate confocal microscope with 488 nm, the maximum illumination power on the skin surface turns out to be 12 milliwatts. This is over a large defocussed spot of diameter ~180 μm, since the focussed illumination spot is actually 100 μm deep (figure 3b), and thus the illumination itself does not cause photodamage to the skin. There is experimental evidence, based on examination of the histology of imaged skin specimens, which shows no damage to the tissue morphology.

Topically applied fluorescein and fluorescein-compounds have proven to be useful for confocal imaging studies of human skin *in vivo*. Current areas of research include morphology and permeability of the corneocyte layers within the stratum corneum (figures 5, 6 and 7).

5.2 Fluorescein isothiocyanate isomer I (FITC-ISOMER I), conjugated to a polymer carrier, in phosphate buffered saline (PBS) solution

FITC-Isomer I (molecular weight 389), has the following properties: excited singlet state lifetime τ_f = 3.8 nsec (emission rate $k_f = 2.6 \times 10^8$ photons/molecule-second), molar extinction coefficient ε = 68000 liters/Mole-cm that is equivalent to an absorbing cross-section $\sigma = 2.6 \times 10^{-16}$ cm^2/molecule, quantum yield η = 0.71, peak excitation wavelength λ_{ex} = 490 nm and peak emission wavelength λ_{em} = 519-525 nm.

Here, we have 1.3×10^5 molecules in the imaged confocal spot volume, and consequently, under excited singlet steady state conditions ($k_a = k_f$), the detected maximum signal is 6400 photons/pixel. The optimum irradiance for maximum signal is calculated to be 4.1×10^5 Watts/cm^2 within the

microvasculature that is equivalent to 1.3 milliwatts. Assuming, again, the blood vessels to be 100 μm deep in the dermis, the optimum illumination power on the surface of the skin is 16 milliwatts over the defocussed spot of diameter ~180 μm. FITC-Isomer I is certainly observable at video-rate with a confocal microscope, as demonstrated by experimental results showing microvasculature and blood flow in Sprague-Dawley rats (figure 8).

5.3 Rhodamine B sulfonyl chloride, conjugated to a polymer carrier, in PBS solution

Rhodamine B sulfonyl chloride (molecular weight 577) has the following properties: excited singlet state lifetime $\tau_f = 1.0$ nsec (i.e., emission rate $k_f = 10^9$ photons/molecule-second), molar extinction coefficient $\varepsilon = 93000$ liters/Mole-cm that is equivalent to an absorbing cross-section $\sigma = 3.6 \times 10^{-16}$ cm^2/molecule, quantum yield $\eta = 0.25$, peak excitation wavelength $\lambda_{ex} = 577$ nm and peak emission wavelength $\lambda_{em} = 590$ nm.

In this case, we have 9.1×10^4 molecules in the imaged confocal spot volume, and again, assuming excited singlet steady state conditions, the detected maximum signal is determined to be 5800 photons/pixel. The optimum irradiance is 11×10^5 Watts/cm^2 within the microvasculature, which corresponds to 3.8 milliwatts, and the optimum illumination power on the skin surface turns out to be 47 milliwatts. Compared to FITC-Isomer I, slightly less fluorescence is expected from Rhodamine B sulfonyl chloride. However, the experimental images indicate a rather poor signal, probably because the illumination wavelength was far away from that for peak absorbance (figure 9). Moreover, the dosage was two orders of magnitude less than (and unnecessarily too far below) the toxic level. This is

a good example of detected signal and image quality being unnecessarily compromised because of sub-optimal experimental parameters.

5.4 Red-shifted green fluorescent protein (GFP) in PBS-and-protein solution

Red-shifted GFP (molecular weight 27000) in PBS-and-protein solution has the following properties: excited singlet state lifetime $\tau_f = 3$ nsec, emission rate $k_f = 2.1 \times 10^8$ photons/molecule-second, molar extinction coefficient $\varepsilon = 39200$ liters/Mole-cm that is equivalent to an absorbing cross-section $\sigma = 1.5 \times 10^{-16}$ cm^2/molecule, quantum yield $\eta = 0.66$, peak excitation wavelength $\lambda_{ex} = 490$ nm and peak emission wavelength $\lambda_{em} = 510$ nm.

The expressed amount of GFP within the tissue is usually not known, but assuming the concentration to be in the range 1 μM-1mM, we expect $3.6 \times 10^3 - 3.6 \times 10^6$ molecules in the imaged confocal spot volume. (This range of concentration was assumed on the basis of measured expression in cultured cells [87].) Assuming, again, excited singlet steady state conditions ($k_a = k_f$), the detected signal is expected to be $1.3 \times 10^2 - 1.3 \times 10^5$ photons/pixel when detecting at 100 μm depth in the dermis. For the more likely experiment of imaging cells within the superficial epidermis, at a depth of, say, 50 μm, the detected signal will be in the range of $10^3 - 10^6$ photons/pixel. GFP is well known to be a stable fluorophore, with a photobleaching rate (k_b) that is about seven-fold smaller than that of fluorescein. This gives $k_b \sim 470$ per second which means that the photobleaching time is ~2100 μsec. Since this is much longer than the dwell time (i..e., illumination time) per pixel of 100 nsec for video-rate scanning, photobleaching does not occur. The optimum irradiance for maximum signal is then calculated to be 5.7×10^5 Watts/cm^2 that, over the diffraction-limited spot diameter of 0.65 μm, is equivalent to 1.9

milliwatts. Under these conditions, the expression of GFP in the keratinocytes within the epidermis of a mouse was experimentally observed with about 2 milliwatts of illumination (figure 10).

5.5 Benzoporphyrin derivative-monoacid ring A (BPD-MA) in methanol

BPD-MA (molecular weight 720) in methanol is a photodynamic drug with the following properties: emission rate $k_f = 1.9 \times 10^8$ photons/molecule-second, molar extinction coefficient ε = 15000-32000 liters/Mole-cm at wavelengths 488 nm-690 nm (equivalent absorbing cross-section $\sigma = 1.2 \times 10^{-16}$ cm^2/molecule at 690 nm), excited singlet state lifetime $\tau_f = 5.2$ nsec, quantum yield $\eta = 0.05$, intersystem crossing efficiency $\eta_{ISC} = 0.8$, triplet state lifetime $\tau_T = 25$ μsec, peak excitation wavelength in the red $\lambda_{ex} = 690$ nm and peak emission wavelength $\lambda_{em} = 695$ nm.

The typical dosage in a small animal such as a rat is 0.25-4.0 mg/kg. Here, we assume 1 mg/kg which yields 7.2×10^4 molecules in the confocal spot volume. Under excited singlet steady state conditions, the maximum detected signal is only 200 photons/pixels. Increasing the dosage to 4 mg/kg will yield 800 photons/pixel. BPD-MA has a high intersystem crossing efficiency, and hence the triplet state will fill up at a fairly fast rate ($k_T = 7.6 \times 10^4$ per second), within only 13 nsec. Since the triplet state fills up much faster than, and subsequently has a lifetime (25 μsec) much longer than, the video-rate pixel time of 100 nsec, the fluorescence emission ceases. Our experimental attempts have, in fact, confirmed this prediction; BPD-MA could not be confocally imaged at high resolution and at video-rate in rat tumor microvasculature.

These experimental examples show that the approximate analysis based on equations (12)-(23) provides a reasonably good prediction of detectability of a given fluorophore within tissue *in vivo* when imaging in real-time with a confocal microscope. Conversely, one can use the analysis to choose fluorophores and optimize the microscope and design experiments for various applications.

6. Instrumentation trade-offs and optimization for signal detectability

The analysis and experimental results lead to an obvious conclusion: detection of fluorescence in a point-scanning confocal microscope may be limited by small imaged spot volumes and short pixel times when imaging at very high resolution (μm-level) and very high speed such as at video-rate (100 nsec). Increasing the laser illumination power will increase the fluorescence emission signal until either the excited singlet- or triplet- states are saturated or photobleaching occurs. Photodamage to the tissue also limits the maximum illumination power that may be used. However, increased fluorescence detectability is possible via trade-offs in optical design and imaging parameters. One obvious factor is the careful choice of high quality optics to maximize light throughput; two especially important components are (i) objective lenses (their NAs versus transmission) to maximize light collection and transmission, and (ii) excitation and detection filters (their wavelength bandwidths versus transmission) to maximize light detection. In general, but especially for fluorophores with small Stokes shifts, the detection bandwidth should be as wide as possible even if it means using shorter wavelengths that are away from the peak absorbance wavelength. The reduced absorbance may usually be compensated for with increased illumination power, until the limit of excited state saturation, photobleaching or photodamage.

For improving detectability and signal-to-noise ratio, other factors to trade-off are resolution that relates to the imaged spot volume, imaging speed (frame rate) that relates to the detector integration time (pixel time), point- versus line- scanning, and mechanical tissue-to-microscope coupling.

6.1 Resolution and imaged confocal spot volume

The resolution and imaged volume is defined by the objective lens NA and detector aperture (pinhole) diameter. High lateral resolution (small illumination spot diameter, small Δx) and high axial resolution (thin section, small Δz) results in the detection of a small number of fluorophore mocleules within a small imaged confocal volume (equation (20)). Although the above analysis and experimental results are for the high NA of 0.9, a lower NA is often acceptable in many living tissue experiments. For nuclear and cellular detail, NAs as low as 0.7 may be used [21, 61, 62], that provide diffraction-limited sectioning of ~2 μm at 488 nm with a water immersion objective lens (this will degrade to ~3-5 μm deep within tissue due to spherical aberration and if large pinholes are used). In rabbit corneal wounds, NA of 0.6 with measured ~9 μm sectioning was adequate for observing cellular structure [16]. Tissue architecture, microvasculature and blood flow may be imaged with NAs as low as 0.3 (diffraction-limited sectioning ~10 μm). Such low NAs have been used to visualize microcirculation in rat brain [2], mouse skin [7] and rat colon [20-22]. Even NA on the order of 0.1 has proven useful to image the pharmacokinetics of drug delivery and distribution in relatively thick sections in rat tumors. Dry objective lenses and pinhole diameters of 5-15 resels (or v = 8-25 optical units) provided sectioning of ~300 μm-1 mm (both calculated and experimentally measured) that were quite useful to investigate photodynamic drugs such as BPD-MA (figure 11) and chlorin-e6 [88], among others.

Here, the trade-off is that lower NAs image larger spots and thicker sections and thus an increased confocal volume (equation (20)) but the collection efficiency decreases (equation (22)). The reduced collection efficiency is, to some extent, compensated for by the higher transmission of objective lenses that have low NAs. Since both sectioning (equation (7)) and collection efficiency (equation (22)) increase quadratically with NA, whereas the sectioning decreases somewhat linearly with pinhole diameter [equation (9); 41, 53], a better option is to use a somewhat higher NA than necessary (say, 0.5-0.3 instead of 0.3-0.1) to improve collection efficiency and then use a larger pinhole to increase the imaged volume while sacrificing some of the unnecessary sectioning and lateral resolution.

6.2 Frame-rate and detection integration time (pixel time)

Although we built a video-rate (30 frames/sec) confocal microscope, our experience in both animal and human studies clearly indicates that video-rate is, in fact, often not necessary for *in vivo* imaging. Imaging at one-fourth to one-third video-rate (i. e., 7-10 frames/sec) is adequate, provided tissue motion is minimized and the imaging site kept stable relative to the objective lens. Consequently, 3-4 video-rate frames may be integrated with a corresponding increase in detected fluorescence signal. The quantum-limited signal-to-noise ratio would decrease as the square-root of the detection integration time [equivalently, √(number of integrated frames)].

Slow frame rates of 1-16 frames/sec over fields-of-view varying from 48x32 to 768x512 pixels have been reported for viewing microcirculation in rat brain cortex [3-6], in skin [7] and in colon, too [20-22]. The resulting detector integration times are long, in the range 1-40 μsec/pixel. Of course, the increase in signal detectability is obtained at a price: there is a corresponding loss of temporal

resolution. Some of the temporal resolution may be regained by imaging a single line instead of a full frame; for example, Dirnagl et al. [5] and Villringer et al. [6] have employed a method of sequentially scanning a single line, of duration 2 msec, that is oriented to be parallel to a blood vessel, to observe moving cells within. The sequence of captured lines is then displayed as a space-time plot from which average blood flow is computed. More recently, line-scanning over full fields-of-view has been effectively used to image morphology and microcirculation.

6.3 Line scanning

Longer detector integration times (pixel times) can be obtained at the expense of resolution with a line-scanning confocal microscope, in which an illumination line is scanned [89-93]. Consider a frame to consist of 500 lines with each line containing 500 pixels: with point scanning, for video-rate imaging (30 frames/sec), the pixel time is ~100 nsec, but when a line is scanned at 30 Hz, assuming non-interlaced frames, we obtain video-rate imaging with pixel time of ~65 μsec.

Compared to point scanning, there is loss of circular symmetry and lateral and axial (sectioning) resolution along the line [32], but the sectioning is adequate to visualize nuclear and cellular detail in various tissues. The sectioning is especially well suited for imaging gross tissue morphology including microvasculature and blood flow. The advantages of a line scanner are that it is simple to build and optimize, has higher light throughput, and uses a standard array detector such as a CCD camera. The detectability in terms of signal-to-noise ratio of a line-scanner, as compared to a point-scanner, is described by Sheppard et al. [57].

A line-scanning fiber-based confocal microendoscope has demonstrated visualization of peritoneum and other tissues through abdominal incisions in mice, at 4 frames/sec, with measured lateral resolution of ~3 μm and section thickness of ~10 μm [23, 24]. Lin recently built a video-rate line scanner, adapted from Brakenhoff et al.'s bilateral design [91, 92], to visualize microcirculation including rolling, adhesion and leukocyte-endothelium interaction in mice [Charles Lin, Dermatology-Wellman Labs., Massachusetts General Hospital, personal communication, 2002]. Koester [89, 90] developed line scanning with a split objective lens aperture: one half of the aperture is used to illuminate and the other half to detect, such that the illumination and detection paths are at an angle to each other, and their intersection precisely defines the confocal section thickness. Although this design has produced remarkable images of nuclear and cellular detail in corneal tissue *in vivo* in reflectance, it has yet to be used in fluorescence (to the best of the authors' knowledge); however, the method has been used to measure the diffusion of fluorophores across excised rabbit cornea specimens [94].

6.4 Wide-field imaging methods

To obtain detection times that are even longer than those from line-scanning, it may be possible to implement wide field imaging methods that provide optical sectioning. When used at video-rate (30 frames/sec), the detection integration time would be the standard 33 msec per frame. Two techniques, one based on deconvolution and the other on structured illumination, have been successfully used for confocal fluorescence imaging of cell cultures *in vitro* and may perhaps find use in tissue *in vivo* (at least in superficial layers, if not deeper layers).

Deconvolution microscopy is a technique in which a stack of blurred images obtained with a conventional microscope are deconvolved with the microscope's PSF to obtain deblurred images of the in-focus planes [95, 96]. The images may be recorded in real-time but the subsequent deconvolution may require seconds to hours. (This processing time has been reducing and will surely reduce more with the availability of increasingly faster computing power.) Thus, morphology may be visualized but not dynamic events such as blood flow. An interesting possibility is to use confocal reflectance imaging with a wavelength that does not excite the fluorophore, to view and locate the site of interest, followed by recording stacks of fluorescence images for deconvolution.

The structured illumination technique is an innovative technique developed by Wilson and his group [97, 98], to obtain confocal sectioning with a conventional microscope that is used in its standard configuration to image a wide field-of-view. Optical sectioning is obtained from a conventional microscope based on the fact that all non-zero spatial frequencies in the object transfer function attenuate with defocus (only the zero spatial frequency does not). By superimposing a specific spatial frequency on the object, one thus obtains contrast-attenuation with defocus (i. e., sectioning). Wilson et al. [98] have presented methods to superimpose a single-spatial frequency grid pattern onto cells in culture , and subsequent removal of the grid pattern, to obtain sectioned fluorescence images of the cells. The superimposition of such a grid pattern within the superficial layers of tissue and imaging with a conventional microscope may provide sectioning in the wide field-of-view images.

6.5 Mechanical tissue-to-microscope coupling

To enable slower imaging speeds (low frame rates), the tissue motion relative to the objective lens must be minimized. Fixtures have been devised to mechanically couple the tissue to the objective lens that first precisely locate the site to be imaged and then keep it stable. One that works particularly well on skin is a contact device consisting of a ring-and-template that is first attached to the tissue (with medical-grade adhesive) and then locks into a housing around the objective lens [61, 62]; this was modified and effectively used to stabilize other tissues *in vivo* such as human oral mucosa [99] and, in small animals, intrasurgically exposed bladder [100], pancreas [101], liver, kidney and other organs. A similar contact device was developed and used for skin by Corcuff et al. [102]. Another method that works well for stabilizing the cornea employs special objective lenses with a dipping cone as the contact element [90]. The dipping cones have been designed such that the curvature of their contact end-surface matches that of the corneal surface; thus, the dipping cone stabilizes the corneal surface by gently pressing against it. Other methods include coverslip-glass windows and specialized fixtures that are implanted within the tissue; examples include those in the cranium to observe microvascular blood flow in the brain cortex [3] and in bone [8]. Boyde et al. [8] also designed objective lenses with a nose cone that engaged into a conical receptacle in the implanted fixtures. The design of fixtures and objective lenses that are specialized to stabilize different tissues thus becomes an important factor for real-time *in vivo* confocal imaging.

Blurring due to tissue motion may also be minimized by triggering frame capture from the motion due to respiration or pulse. However, this distorts the confocal plane, especially when imaging at slow frame rates, since the tissue moves during the frame capture. Despite the distortion, this triggering method has proven to be useful; Villringer et al. [3, 4] have managed to capture up to ten single frames over ten respiration cycles (each cycle 0.75-1 sec long), and then sum the frames with fairly minimal

blurring in rat brain cortex. The distortion may be minimized by using faster frame rates, and compensating for the loss of signal by summing a larger number of frames.

7. Summary and conclusions

With careful analysis and attention to experimental detail, it is often possible to detect fluorescence in living tissue in real-time (including video-rate in many cases) with a confocal microscope. We expect significantly improved detectability and higher-quality imaging than that presented in this chapter, if well-designed microscopes are developed and the experimental parameters are well-optimized. One must use an analytical model for *in vivo* confocal fluorescence imaging studies; the analysis may be either approximate (as shown here) or more detailed (that can be developed from the available literature). The analysis will allow one to design the confocal optics for maximum light throughput and optimum imaging parameters. Application-specific choices must be made for fluorophore and its concentration, resolution (imaged volume), frame rate (pixel time) and scanning method (resolution versus pixel time). The analytical results should be validated with calibration experiments on excised tissue (*ex vivo*) or *in vitro* specimens; this is often useful to estimate optimum instrumentation and imaging parameters for the actual *in vivo* experiments. For *in vivo* applications, imaging at video-rate is not always necessary; imaging at much slower speeds (say, $1/4^{th}$ or $1/3^{rd}$ video-rate or 7-10 frames/sec) may be performed, provided the tissue is well stabilized. The relative motion between the tissue and the objective lens must be minimized to within $\approx \pm 1$ cell (or better); this requires specially designed objective lenses and lens-to-tissue contact devices that are specific to the shape and structure of the tissue. The question of fluorophore-induced toxicity and the mechanism and extent of photodamage in tissues *in vivo* during confocal imaging is largely unanswered; this calls for a detailed

investigation of the effects of illumination and flurophore on living tissue morphology and function. Visible illumination wavelengths have limited the maximum depth of imaging to 100-200 μm in tissues. Deeper imaging, down to 200-500 μm, should be possible with the advent of near-infrared fluorophores that would allow the use of longer illumination wavelengths. Confocal fluorescence imaging of animal and human tissues *in vivo* remains to be fully exploited for basic and clinical research.

8. References

This list of references has been selected as representative of the literature, and is by no means exhaustive. For an exhaustive list, we recommend a MEDLINE and INSPEC search using the keywords confocal fluorescence microscopy, imaging, real-time, video-rate, in vivo, animal, human, living tissue, skin, blood, tumor, etc.

The abbreviation HBCM is used for: JB Pawley, ed. Handbook of Biological Confocal Microscopy, New York: Plenum Press. (This is reference 33.) Two editions of this book are referenced: revised ed., 1990 and 2nd ed., 1995.

1. M Minsky. Microscopy Apparatus, US Patent 3013467 (filed 7 Nov 1957), 1961.

2. A Villringer, RL Haberl, U Dirnagl, F Anneser, M Verst, KM Einhaupl. Confocal laser microscopy to study microcirculation on the rat brain surface *in vivo*. Brain Res 504: 159-160, 1989.

3. A Villringer, U Dirnagl, A Them, L Schurer, F Krombach, KM Einhaupl. Imaging of leukocytes within the rat brain cortex *in vivo*. Microvasc Res 42: 305-315, 1991.

4. U Dirnagl, A Villringer, R Gebhardt, RL Haberl, P Schmiedek, KM Einhaupl. Three-dimensional reconstruction of the rat brain cortical microcirculation *in vivo*. J Cerebr Blood Flow and Metab 11: 353-360, 1991.

5. U Dirnagl, A Villringer, KM Einhaupl. *In-vivo* confocal scanning laser microscopy of the cerebral microcirculation. J Microsc 165: 147-157, 1992.

6. A Villringer, A Them, U Lindauer, K Einhaupl, U Dirnagl. Capillary perfusion of the rat brain cortex – an *in vivo* microscopical study. Circ Res 75: 55-62, 1994.

7. LJ Bussau, LT Vo, PM Delaney, GD Papworth, DH Barkla, RG King. Fiber optic confocal imaging (FOCI) of keratinocytes, blood vessels and nerves in hairless mouse skin *in vivo*. J Anat 192: 187-194, 1998.

8. A Boyde, LA Wolfe, M Maly, SJ Jones. Vital confocal microscopy in bone. Scanning 17: 72-85, 1995.

9. A Boyde, SJ Jones, ML Taylor, LA Wolfe, TF Watson. Fluorescence in the tandem scanning microscope. J Microsc 157: 39-49, 1990.

10. H Ichijima, WM Petroll, JV Jester, HD Cavanagh. Confocal microscopic studies of living rabbit cornea treated with benzalkonium chloride. Cornea 11: 221-225, 1992.

11. SJ Jones, ML Taylor. Confocal fluorescence microscopy: some applications in bone cell biology. J Microsc 158: 249-259, 1990.

12. A Boyde, G Capasso, RJ Unwin. Conventional and confocal epi-reflection and fluorescence microscopy of the rat kidney in vivo. Exp Nephrol 6: 398-408, 1998.

13. J Kishimoto, R Ehama, Y Ge, T Kobayashi, T Nishiyama, M Detmar, RE Burgeson. In vivo detection of human vascular endothelial growth factor promoter activity in transgenic mouse skin. Am J Pathol 157: 103-110, 2000.

14. J Kacza, J Grosche, J Seeger, K Brauer, G Bruckner, W Hartig. Laser scanning and electron microscopic evidence for rapid and specific in vivo labelling of cholinergic neurons in the rat basal forebrain with fluorochromated antibodies. Brain Res 867: 232-238, 2000.

15. SE Ilyin, MC Flynn, CR Plata-Salaman. Fiber-optic monitoring coupled with confocal microscopy for imaging gene expression in vitro and in vivo. J Neurosci Methods 108: 91-96, 2001.

16. T Moller-Pedersen, HF Li, WM Petroll, HD Cavanagh, JV Jester. Confocal microscopic characterization of wound repair after photorefractive keratectomy. Invest Ophthalmol Vis Sci 39: 487-501, 1998.

17. FA Merchant, SJ Aggarwal, KR Diller, AC Bovik. In-vivo analysis of angiogenesis and revascularization of transplanted pancreatic islets using confocal microscopy. J Microsc 176: 262-275, 1994.

18. PJ White, RD Fogarty, IJ Liepe, PM Delaney, GA Werther, CJ Wraight. Live confocal microscopy of oligonucleotide uptake by keratinocytes in human skin grafts on nude mice. J Invest Dermatol 112: 887-892, 1999.

19. PM Delaney, MR Harris, RG King. Fiber-optic laser scanning confocal microscope suitable for fluorescence imaging. Appl Opt 33: 573-577, 1994.

20. PM Delaney, RG King, JR Lambert, MR Harris. Fiber optic confocal imaging (FOCI) for subsurface microscopy of the colon in vivo. J Anat 184: 157-160, 1994.

21. GD Papworth, PM Delaney, LJ Bussau, LT Vo, RG King. In vivo fiber optic confocal imaging of microvasculature and nerves in the rat vas deferens and colon. J Anat 192: 489-495, 1998.

22. W McLaren, P Anikijenko, D Barkla, TP Delaney, R King. *In vivo* detection of experimental ulcerative colitis in rats using fiberoptic confocal imaging (FOCI). Dig Dis Sci 46: 2263-2276, 2001.

23. YS Sabharwal, AR Rouse, L Donaldson, MF Hopkins, AF Gmitro. Slit-scanning confocal microendoscope for high-resolution *in vivo* imaging. Appl Opt 38: 7133-7144, 1999.

24. AF Gmitro, AR Rouse, YS Sabharwal. In situ optical biopsy with a confocal microendoscope. Proc of the 22nd Annual EMBS Intl Conf, Chicago, 2000, pp 1040-1042.

25. AJ Mueller, WR Freeman, R Folberg, DU Bartsch, A Scheider, U Schaller, A Kampik. Evaluation of microvascularization pattern visibility in human choroidal melanomas: comparison of confocal fluorescein with indocyanine green angiography. Graefes Arch Clin Exp Ophthalmol 237: 448-456, 1999.

26. I Foissner, D Wendehenne, C Langebartels, J Durner. In vivo imaging of an elicitor-induced nitric oxide burst in tobacco. Plant J 23: 817-824, 2000.

27. JP Verbelen, S Kerstens. Polarization confocal microscopy and congo red fluorescence: a simple and rapid method to determine the mean cellulose fibril orientation in plants. J Microsc 198: 101-107, 2000.

28. B Hedtke, M Meixner, S Gillandt, E Richter, T Borner, A Weihe. Green fluorescent protein as a marker to investigate targeting of organellar RNA polymerases of higher plants in vivo. Plant J 17: 557-561, 1999.

29. RH Kohler, WR Zipfel, WW Webb, MR Hanson. The green fluorescent protein as a marker to visualize plant mitochondria in vivo. Plant J 11: 613-621, 1997.

30. GJ Brakenhoff, K Visscher. Chapter 21, Real-time stereo (3D) confocal microscopy. In: HBCM, 1995, pp. 355-362.

31. T Wilson, CJR Sheppard. Theory and Practice of Scanning Optical Microscopy. New York: Academic Press, 1984.

32. T Wilson, ed. Confocal Microscopy. San Diego: Academic Press, 1990.

33. JB Pawley, ed. Handbook of Biological Confocal Microscopy, 2nd ed. New York: Plenum Press, 1995.

34. RH Webb. Confocal optical microscopy. Rep Prog Phys 59: 427-471, 1996.

35. M Born, E Wolf. Principles of Optics, 6th ed. New York: Pergamon Press, 1991.

36. JW Goodman. Introduction to Fourier Optics. New York: McGraw-Hill, 1968.

37. CJR Sheppard, A Choudhury. Image formation in the scanning microscope. Opt Acta 24: 1051-1073, 1977.

38. GJ Brakenhoff, P Blom, P Barends. Confocal scanning light microscopy with high aperture immersion lenses. J. Microsc 117: 219-232, 1979.

39. T Wilson, AR Carlini. Three-dimensional imaging in confocal imaging systems with finite sized detectors. J Microsc 149: 51-66, 1988.

40. CJR Sheppard. Super-resolution in confocal imaging. Optik 80: 53-54, 1988.

41. GJ Brakenhoff, HTM van der Voort, EA van Spronsen, N Nanninga. Three-dimensional imaging in fluorescence by confocal scanning microscopy. J. Microsc 153: 151-159, 1989.

42. HTM van der Voort, GJ Brakenhoff. Three-dimensional image formation in high-aperture fluorescence confocal microscopy: a numerical analysis. J Microsc 158: 43-54, 1990.

43. GJ Brakenhoff, K Visscher, HTM van der Voort. Chapter 8, Size and shape of the confocal spot: control and relation to 3D imaging and image processing. In: HBCM, 1990. pp. 87-91.

44. IJ Cox, CJR Sheppard, T Wilson. Super-resolution by confocal fluorescence microscopy. Optik 60: 391-396, 1981.

45. RW Wijnaendts-van-Resandt, HJB Marsman, R Kaplan, J Davoust, EHK Stelzer, R Stricker. Optical fluorescence microscopy in three dimensions: microtomoscopy. J Microsc 138: 29-34, 1985.

46. T Wilson. Optical sectioning in confocal fluorescent microscopes. J Microsc 154: 143-156, 1989.

47. CJR Sheppard. Axial resolution of confocal fluorescence microscopy. J Microsc 154: 237-241, 1989.

48. S Kimura, C Munakata. Depth resolution of the fluorescent confocal scanning microscope. Appl Opt 29: 489-494, 1990.

49. T Wilson, SJ Hewlett. Imaging in scanning microscopes with slit-shaped detectors. J Microsc 160: 115-139, 1990.

50. CJR Sheppard, M Gu. Imaging performance of confocal fluorescence microscopes with finite-sized source. J Mod Opt 41: 1521-1530, 1994.

51. O Nakamura. Three-dimensional imaging characteristics of laser scan fluorescence microscopy: two-photon excitation vs. single-photon excitation. Optik 93: 39-42, 1993.

52. V Drazic. Three-dimensional transfer function analysis of a confocal fluorescence microscope with a finite-sized source and detector. J Mod Opt 40: 879-887, 1993.

53. T Wilson. Chapter 11, The role of the pinhole in confocal imaging systems. In: HBCM, 1995, pp. 167-182.

54. M Gu, CJR Sheppard. Effects of a finite-sized detector on the OTF of confocal fluorescent microscopy. Optik 89: 65-69, 1991.

55. M Gu, CJR Sheppard. Confocal fluorescent microscopy with a finite-sized circular detector. J Opt Soc Am A 9: 151-153, 1992.

56. XS Gan, CJR Sheppard. Detectability: a new criterion for evaluation of the confocal microscope. Scanning 15: 187-192, 1993.

57. CJR Sheppard, X Gan, M Gu, M Roy. Chapter 22, Signal-to-noise ratio in confocal microscopes. In: HBCM, 1995, pp. 363-371.

58. RY Tsien, A Waggoner. Chapter 16, Fluorophores for confocal microscopy – photophysics and photochemistry. In: HBCM, 1995, pp. 267-279.

59. DR Sandison, RM Williams, KS Wells, J Strickler, WW Webb. Chapter 3, Quantitative fluorescence confocal laser scanning microscopy (CLSM). In: HBCM, 1995, pp. 39-53.

60. M Rajadhyaksha, M Grossman, D Esterowitz, RH Webb, RR Anderson. *In vivo* confocal scanning laser microscopy of human skin: melanin provides strong contrast. J Invest Dermatol 104: 946-952, 1995.

61. M Rajadhyaksha, RR Anderson, RH Webb. Video-rate confocal scanning laser microscope for imaging human tissues *in vivo*. Appl Opt 38: 2105-2115, 1999.

62. M Rajadhyaksha, S Gonzalez, JM Zavislan, RR Anderson, RH Webb. *In vivo* confocal scanning laser microscopy of human skin II: advances in instrumentation and comparison with histology. J Invest Dermatol 113: 293-303, 1999.

63. HE Keller. Chapter 7, Objective lenses for confocal microscopy. In: HBCM, 1995, pp. 111-126.

64. SW Hell, EHK Stelzer. Chapter 20, Lens aberrations in confocal fluorescence microscopy. In: HBCM, 1995, pp. 347-354.

65. S Hell, G Reiner, C Cremer, EHK Stelzer. Aberrations in confocal fluorescence microscopy induced by mismatches in refractive index. J Microsc 169: 391-405, 1993.

66. H Jacobsen, SW Hell. Effect of the specimen refractive index on the imaging of a confocal fluorescence microscope employing high aperture oil immersion lenses. Bioimaging 3: 39-47, 1995.

67. DS Wan, M Rajadhyaksha, RH Webb. Analysis of spherical aberration of a water immersion objective: application to specimens with refractive indices 1.33-1.40. J Microsc 197: 274-284, 2000.

68. TD Visser, FCA Groen, GJ Brakenhoff. Absorption and scattering correction in fluorescence confocal microscopy. J Microsc 163: 189-200, 1991.

69. AK Dunn. Light scattering properties of cells. Ph. D. thesis, University of Texas, Austin, 1997.

70. AK Dunn, C Smithpeter, AJ Welch, R Richards-Kortum. Finite-difference time-domain simulation of light scattering from single cells. J Biomed Opt 2: 262-266, 1997.

71. WF Cheong, SA Prahl, AJ Welch. A review of the optical properties of biological tissue. IEEE J Quant Electr 26: 2166-2185, 1990.

72. C Saloma, C Palmes-Saloma, H Kondoh. Site-specific confocal fluorescence imaging of biological microstructures in a turbid medium. Phys Med Biol 43: 1741-1759, 1998.

73. DR Sandison, WW Webb. Background rejection and signal-to-noise optimization in confocal and alternative fluorescence microscopes. Appl Opt 33: 603-615, 1994.

74. DR Sandison, DW Piston, RM Williams, WW Webb. Quantitative comparison of background rejection, signal-to-noise ratio, and resolution in confocal and full-field laser scanning microscopes. Appl Opt 34: 3576-3588, 1995.

75. R Gauderon, CJR Sheppard. Effect of a finite-size pinhole on noise performance in single-, two-, and three-photon confocal fluorescence microscopy. Appl Opt 38: 3562-3565, 1999.

76. EHK Stelzer. Contrast, resolution, pixelation, dynamic range and signal-to-noise ratio: fundamental limits to resolution in fluorescence light microscopy. J Microsc 189: 15-24, 1998.

77. M Terasaki, ME Dailey. Chapter 19, Confocal microscopy of living cells. In: HBCM, 1995, pp. 327-346.

78. C Cullander. Chapter 3, Fluorescent probes for confocal microscopy. Methods Mol Biol 122: 59-73, 1999.

79. JC Scaiano, ed. CRC Handbook of Organic Photochemistry, vol I. Boca Raton, FL: CRC Press, 1989.

80. IB Berlman. Handbook of Fluorescence Spectra of Aromatic Molecules, 2nd ed. New York: Academic Press, 1971.

81. SL Murov, I Carmichael, GL Hug. Handbook of Photochemistry, 2nd ed. New York: Marcel Dekker, 1993.

82. W Horspool, P Song, eds. CRC Handbook of Organic Photochemistry and Photobiology. Boca Raton, FL: CRC Press, 1995.

83. RY Tsien. Fluorescent probes of cell signaling. Ann Rev Neurosci 12: 227-253, 1989.

84. RY Tsien. Chapter 5, Fluorescent indicators of ion concentrations. Methods Cell Biol 30: 127-156, 1989.

85. A Waggoner, R DeBiasio, P Conrad, GR Bright, L Ernst, K Ryan, M Nederlof, D Taylor. Chapter 17, Multiple spectral parameter imaging. Methods Cell Biol 30: 449-478, 1989.

86. RF Chen, CH Scott. Atlas of fluorescence spectra and lifetimes of dyes attached to protein. Anal Lett 18: 383-421, 1985.

87. B Herman. Fluorescence Microscopy, 2nd ed. New York: Springer-Verlag, 1998, p. 64.

88. MR Hamblin, M Rajadhyaksha, T Momma, NS Soukos, T Hasan. In vivo fluorescence imaging of the transport of charged chlorin-e6 conjugates in a rat orthotopic prostate tumor. Br J Cancer 81: 261-268, 1999.

89. CJ Koester. Scanning mirror microscope with optical sectioning characteristics: applications to ophthalmology. Appl Opt 19: 1749-1757, 1980.

90. CJ Koester, JD Auran, HD Rosskothen, GJ Florakis, RB Tackaberry. Clinical microscopy of the cornea utilizing optical sectioning and a high numerical-aperture objective. J Opt Soc Am A 10: 1670-1679, 1993.

91. GJ Brakenhoff, J Visscher. Confocal imaging with bilateral scanning and array detectors. J. Microsc 165: 139-146, 1992.

92. GJ Brakenhoff, J Visscher. Imaging modes for bilateral confocal scanning microscopy. J. Microsc 171: 17-26, 1993.

93. WB Amos, JG White. Chapter 25, Direct view confocal imaging systems using a slit aperture. In: HBCM, 1995, pp. 403-416.

94. SP Srinivas, DM Maurice. A microfluorometer for measuring diffusion of fluorophores across the cornea. IEEE Trans Biomed Engr 39: 1283-1291, 1992.

95. WA Carrington, KE Fogarty, L Lifschitz, FS Fay. Chapter 14, Three-dimensional imaging on confocal and wide-field microscopes. In: HBCM, 1990, pp. 151-161.

96. PJ Shaw. Chapter 23, Comparison of wide-field/deconvolution and confocal microscopy for 3D imaging. In: HBCM, 1995, pp. 373-387.

97. MAA Neil, R Juskaitis, T Wilson. Method of obtaining optical sectioning by using structured light in a conventional microscope. Opt Lett 22: 1905-1907, 1997.

98. MAA Neil, A Squire, R Juskaitis, PIH Bastiaens, T Wilson. Wide-field optically sectioning fluorescence microscopy with laser illumination. J Microsc 197: 1-4, 2000.

99. WM White, M Rajadhyaksha, S Gonzalez, RL Fabian, RR Anderson. Noninvasive imaging of human oral mucosa in vivo by confocal reflectance microscopy. Laryngoscope: 109: 1709-1717, 1999.

100. F Koenig, S Gonzalez, WM White, M Lein, M Rajadhyaksha. Near-infrared confocal laser scanning microscopy of bladder tissue in vivo. Urology: 53: 853-857, 1999.

101. T Keck, V Campo-Ruiz, AL Warshaw, RR Anderson, CF Castillo, S Gonzalez. Evaluation of morphology and microcirculation of the pancreas by ex vivo and in vivo reflectance confocal microscopy. Pancreatology 1: 48-57, 2001.

102 P Corcuff, C Chaussepied, G Madry, C Hadjur. Skin optics revisited by in vivo confocal microscopy: melanin and sun exposure. J Cosmet Sci 52: 91-102, 2001.

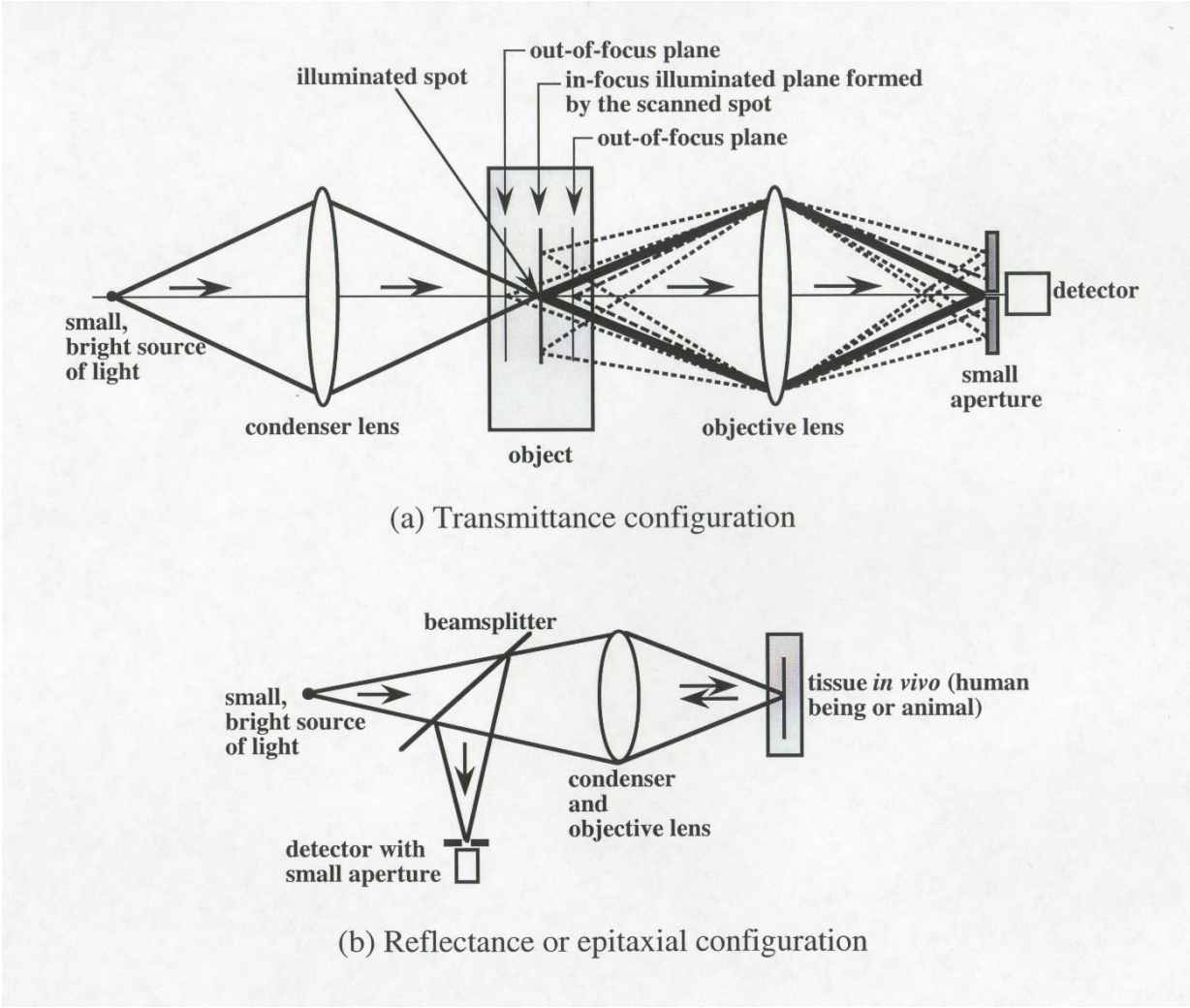

Figure 1. Optical sectioning with a confocal microscope is the imaging of the single specific plane that is in focus within the object (a). A small source of light illuminates a small three-dimensional spot within the object, which is imaged onto a detector through a small aperture (pinhole). The detector receives light only from the illuminated spot that is in focus (bold lines); light from all other spots that are either axially or laterally away from focus is spatially filtered by the aperture in front of the detector (dotted lines). The illuminated spot may be scanned in two dimensions to create an image of a plane; thus, a thin slice or section is noninvasively observed. Illuminating a small spot and imaging through a small detector aperture provides high axial resolution and high contrast (due to

strong rejection of out-of-focus light that, otherwise, would cause blur). Figure (a) shows the transmittance configuration with the illumination light penetrating through the object and being detected on the other side. However, imaging an animal or human being requires detection of back-scattered light in the reflectance (or epitaxial) configuration, with the illumination and detection being on the same side of the tissue (b).

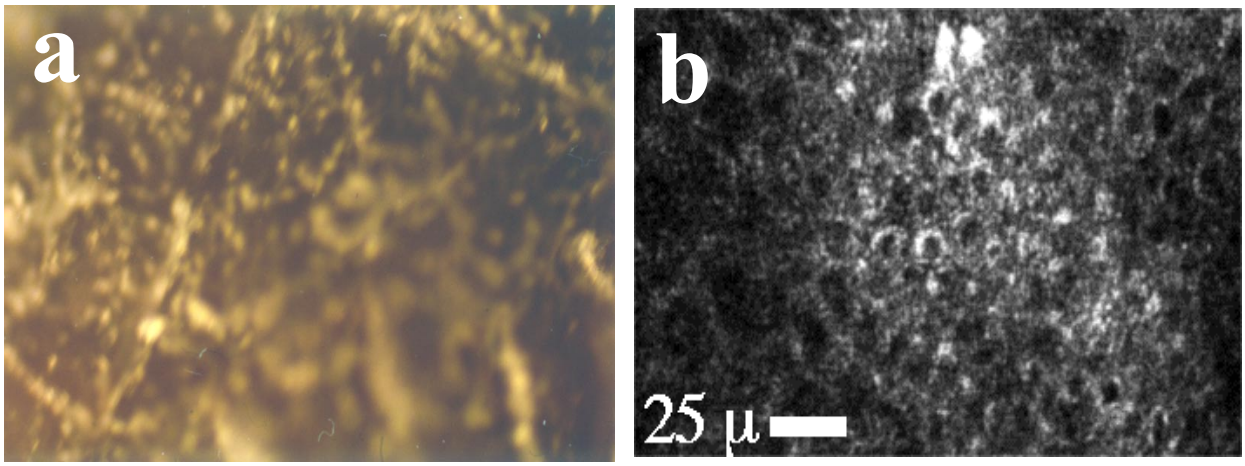

Figure 2. Human skin *in vivo* appears blurred with a conventional microscope (a) but sharp and well-resolved with a confocal microscope (b). The confocal section shows a thin layer of basal cells of diameter ~10 µm and ~70 µm deep within skin. A conventional microscope does not provide axial resolution and lacks optical sectioning capability because a large source of light illuminates a large spot (large volume) within the object, that is imaged onto a detector through a large aperture. The detector receives light from the plane that is in focus as well as planes that are away from focus. (Imagine what would happen when the detector aperture in figure 1(a) is made large.) Consequently, the object has to be physically cut into thin sections and stained before viewing with a conventional microscope.

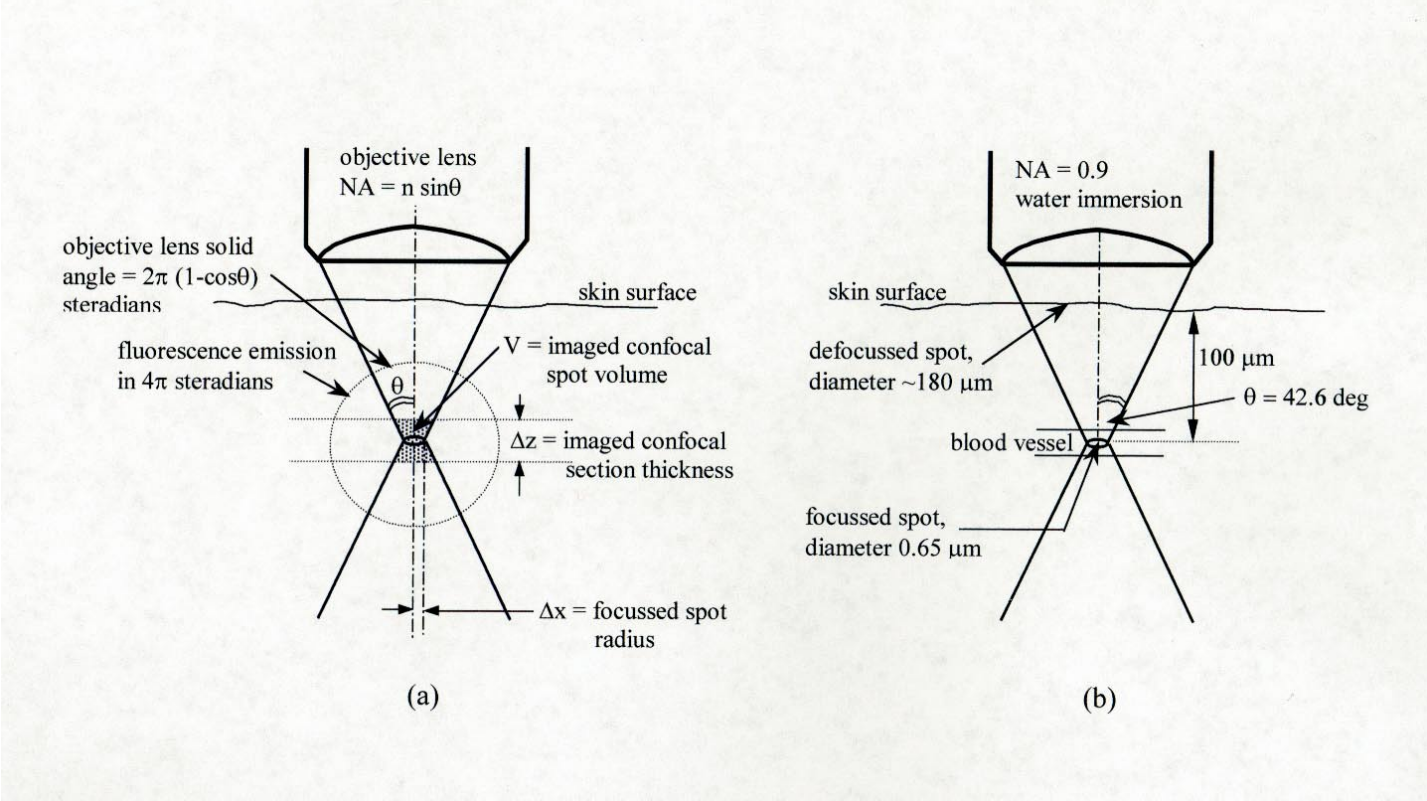

Figure 3. (a) The imaged spot (shaded volume) is defined by the focused cone of light that is within the confocal section, and is of volume V defined by equation (20). The fluorescence emission is assumed to occur uniformly over 4π steradians, whereas the objective lens will collect only that fraction that is within the solid angle defined by its NA. (b) When the focussed spot (of diameter 0.65 μm for 0.9 NA water immersion lens at wavelength 488 nm) is within a blood vessel at a depth of 100 μm, the defocussed spot that is formed by the illumination cone on the skin surface is ~180 μm.

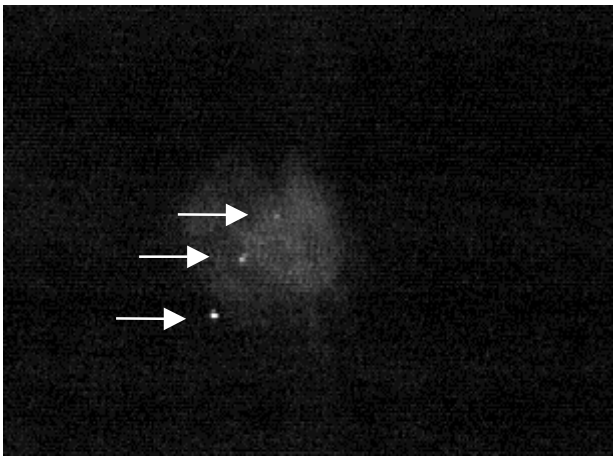

Figure 4. Video-rate confocal image of individual fluorescein-labelled microspheres (arrows) in the microcirculation of a Sprague-Dawley rat. Each microsphere is of diameter 0.5 μm, containing ~10^6 molecules. Objective lens 60X, 0.9 NA water immersion, pinhole diameter 10 resels, excitation at 488 nm, detection through a 520 nm-long pass filter, illumination power 1-5 milliwatts on the skin surface.

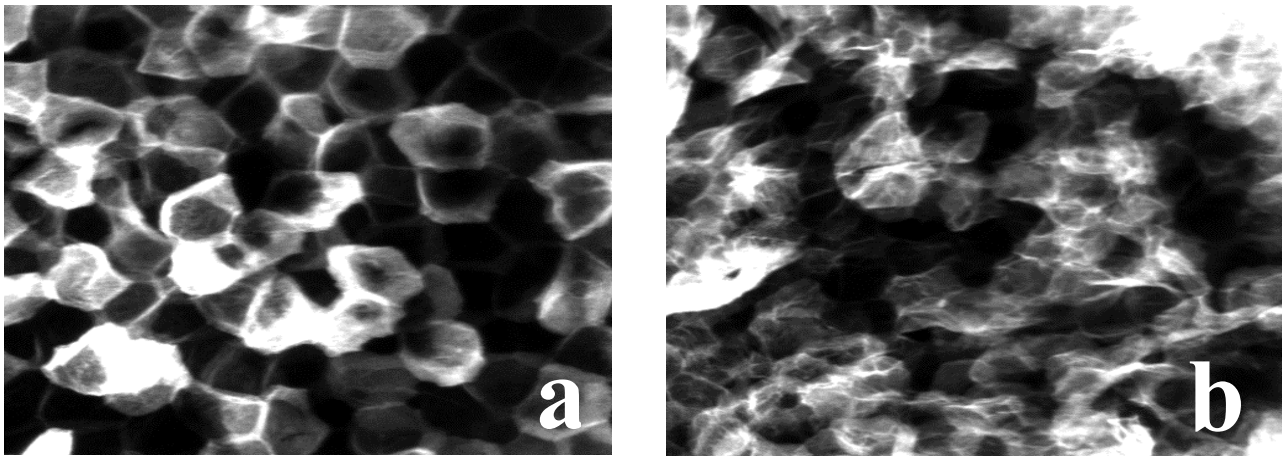

Figure 5. The processes of cornification and desquamation, showing the highly ordered lattice of regular polygonal-shaped corneocytes in healthy skin (a) versus the disordered pattern of irregular-shaped corneocytes in unhealthy skin (b), as imaged with a tandem scanning confocal microscope, following topical application of fluorescein. The images are maximum intensity renderings of stacks

taken at 2.5 μm-intervals between slices. The images were taken with a Nikon 0.75 NA multi-immersion objective set to glycerol (the immersion fluid was sunflower oil which has the same refractive index as glycerol), detector slit width of 10 μm, at video-rate (30 frames/second), 0.5 μm per pixel, and no averaging. The excitation wavelength was 488 nm and detection through a 500 nm long pass filter. The fluorescence contrast is due to the inhomogeneous absorption of fluorescein; the differences in shape, size, spatial distribution and morphology of corneocytes have been quantitatively and qualitatively analyzed from such images. Significant variations in such features are correlated to skin conditions such as age, dryness and disease. Courtesy of Daan Thorn-Leeson, Kumar Subramanyam, K. P. Ananth, Unilever US Research, New Jersey.

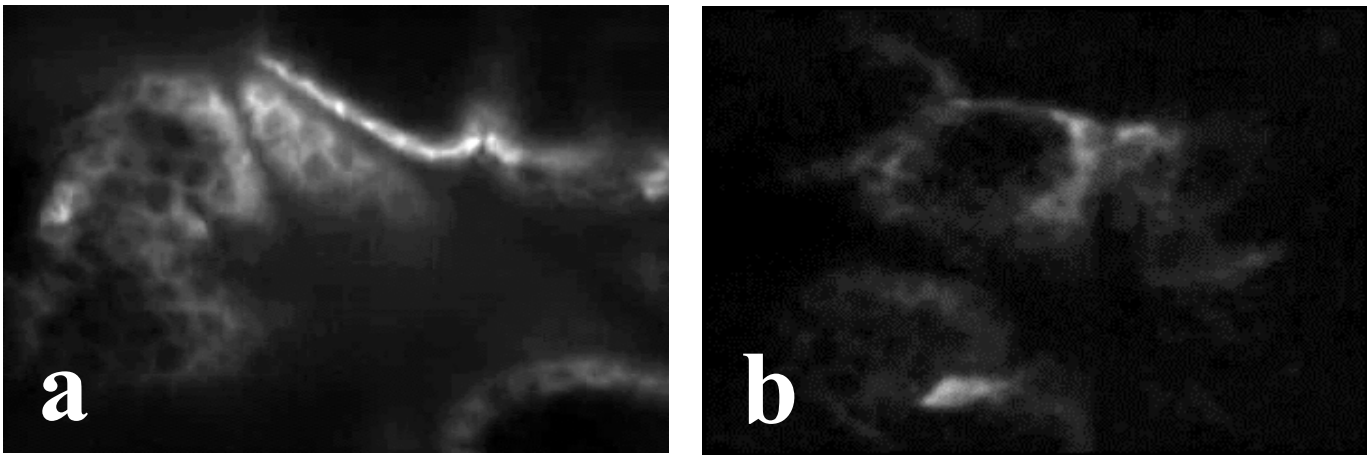

Figure 6. Confocal fluorescence study of the relative penetration of oil- and water-soluble moisturizer/cleanser actives in human stratum corneum *in vivo*: the hydrophobic active labelled with fluorescein octadecyl ester (ODF) remains trapped in the fine wrinkles and grooves on the surface, and is adsorbed in the superficial corneocyte layers (a), whereas the hydrophilic active labelled with fluorescein penetrates through the intercellular spaces to depths of 10-20 μm (b). The actives formulations contained ~200 ppm of the fluorophores, of which ~0.5 ml was applied on a test area of

~3 cm, resulting in an estimated ~10^7 fluorophore molecules in the confocal spot. Objective lens 60X, 0.9 NA water immersion, pinhole diameter 10 resels, excitation at 488 nm, detection through a 520 nm long-pass filter, illumination power 1-5 milliwatts on the skin, averaging of 2-4 video-rate frames. Courtesy of Hung-Ta Chang, K. P. Ananth, Unilever US Research, New Jersey.

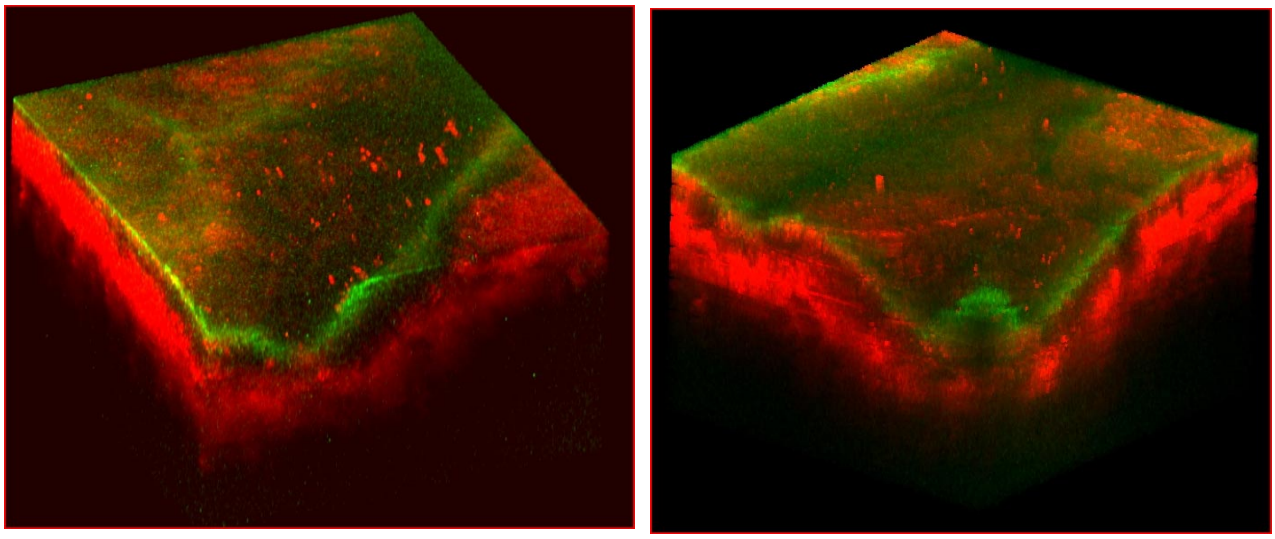

Figure 7 Simultaneous fluorescence and reflectance stacks of human skin *in vivo* following topical application of octadecyl fluorescein (ODF), demonstrating the co-localization of the fluorescence signal in the context of the reflected image. The false-colored green areas indicate the 3D distribution of the dye within the stratum corneum, overlying the false-colored red epidermis and dermis. The stacks were imaged with a Noran Oz super-video rate laser confocal scanner equipped with a contact depth-scanning device. The resolution with high numerical NA objectives (NA = 1.3-1.4) is of the order of $\lambda/2$ laterally and about λ in the axial or depth direction. The instrument can vary its scan rate from 30 frames per second up to 480 frames per second with a reduced format, and the scanner is designed to image simultaneously in fluorescence and reflectance. Courtesy of Ricardo Toledo-Crow, Noran Inc., Middleton, WI.

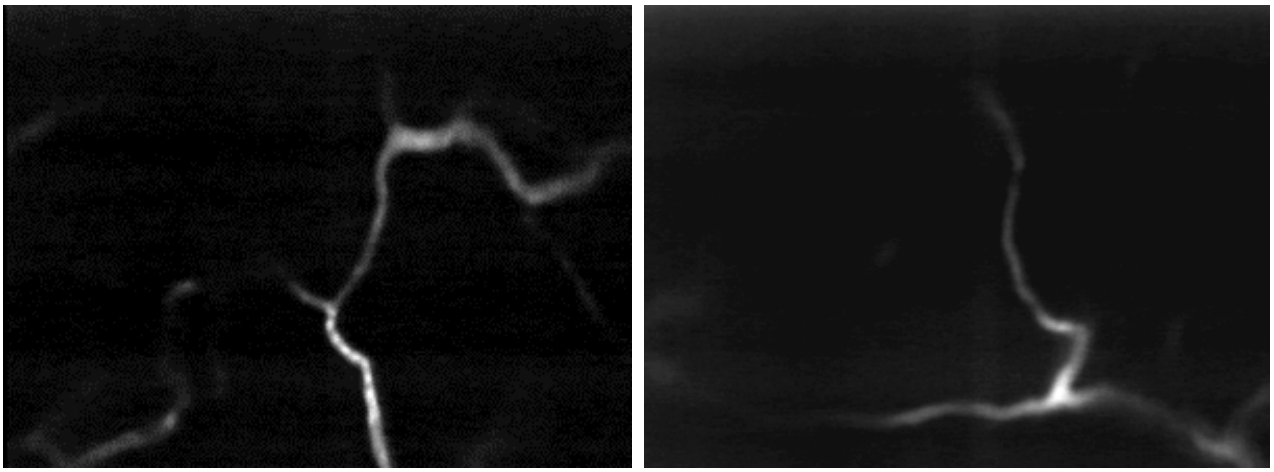

Figure 8. Video-rate confocal fluorescence image of microcirculation in the ear of a Sprague-Dawley rat using FITC-Isomer I conjugated to a polymer carrier, in PBS solution. Imaging parameters: 60X, 0.9 NA water immersion objective lens, excitation wavelength 488 nm, detection through 520 nm long-pass filter, illumination power 10-20 milliwatts on the skin surface, depth ~100 μm, dosage ~1.2 mg/kg injected in the femoral vein (toxic dosage ~100 mg/kg). Dark-appearing circulating blood cells were seen within the bright plasma in real-time. Courtesy of Mark Henrichs, Nycomed-Amersham, Wayne, PA.

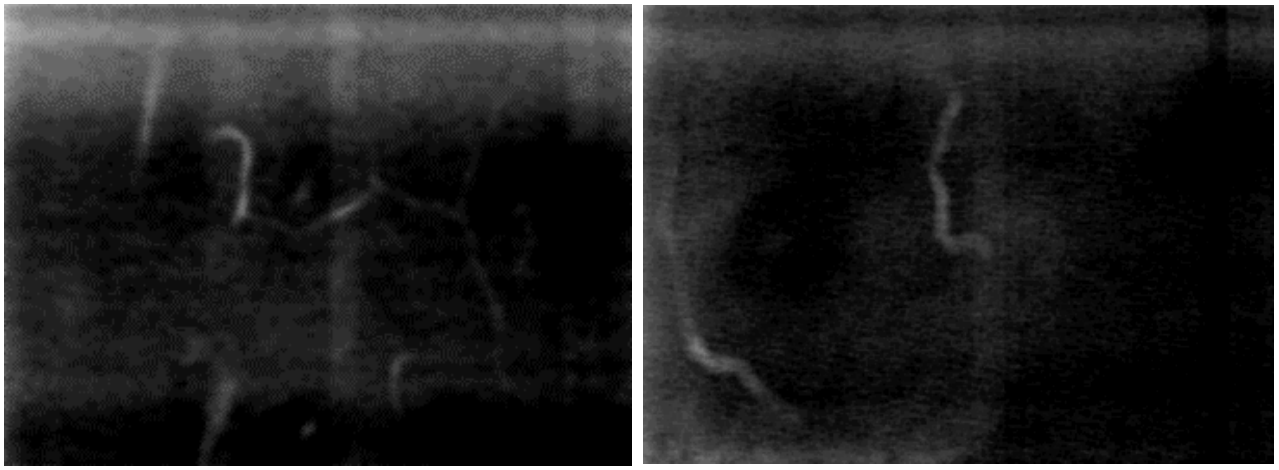

Figure 9. Video-rate confocal fluorescence image of microcirculation in the ear of a Sprague-Dawley rat using Rhodamine B sulfonly chloride conjugated to a polymer carrier, in PBS solution.

Imaging parameters: 60X, 0.9 NA water immersion objective lens, excitation wavelength 488 nm, detection through 540 nm long-pass filter, illumination power 30-60 milliwatts on the skin surface, depth ~100 μm, dosage ~1.6 mg/kg injected in the femoral vein (toxic dosage ~300 mg/kg). The detected signal was poor, probably because the illumination wavelength was far away from the 577 nm for peak absorbance, and moreover, the dosage was unnecessarily too far below the toxic level. This is a good example of how detected signal and image quality was unnecessarily compromised because of sub-optimal experimental parameters. Courtesy of Mark Henrichs, Nycomed-Amersham, Wayne, PA.

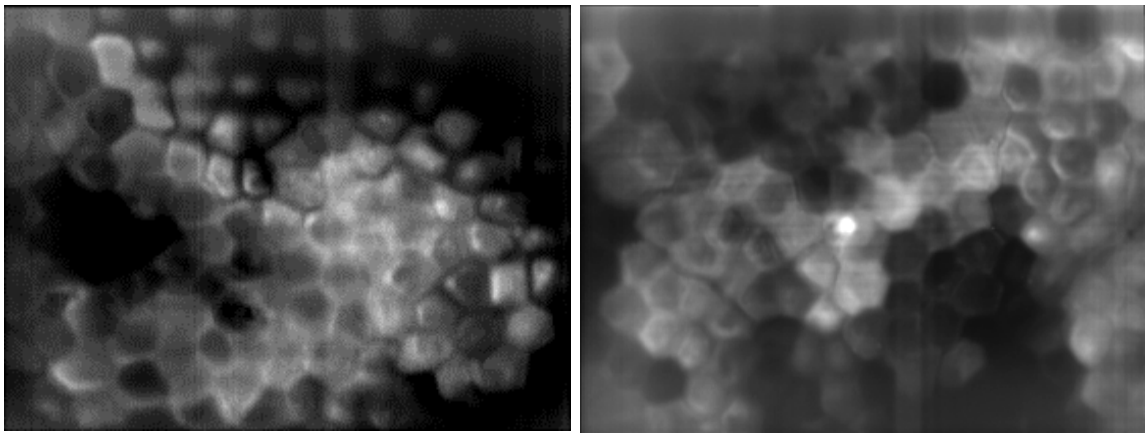

Figure 10. Video-rate confocal image showing the expression of GFP in keratinocytes under the control of VEGF promoter in the epidermis of a transgenic mouse *in vivo*. Objective lens 60X, 0.9 NA water immersion, pinhole diameter 10 resels, excitation at 488 nm, detection through a 510 ± 5 nm band-pass filter, illumination power 2 milliwatts on the skin, no frame averaging. Courtesy of Ramnik Xavier, Department of Molecular Biology, Massachusetts General Hospital, Boston, MA.

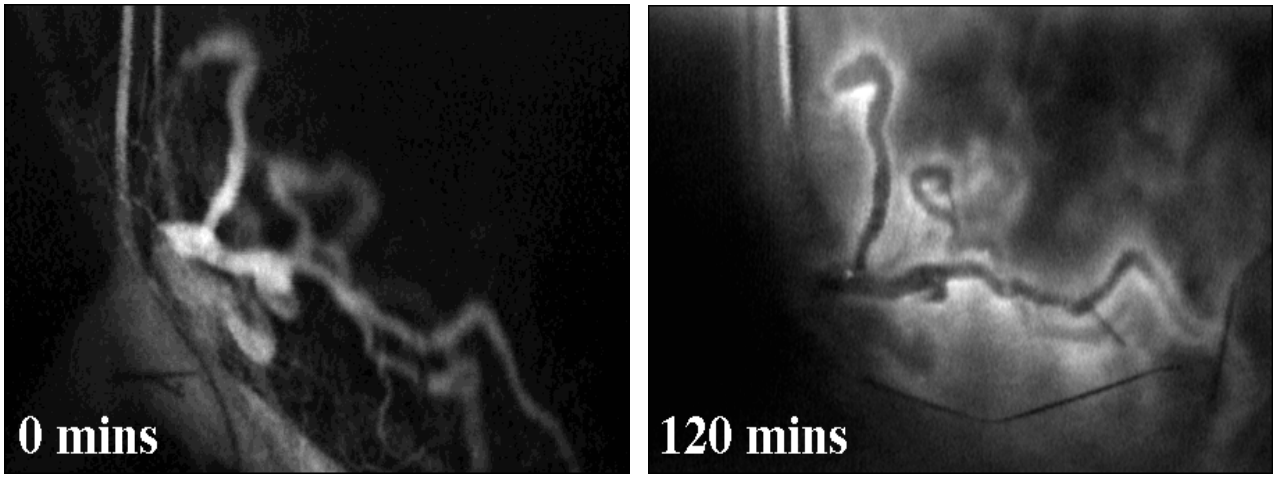

Figure 11. Confocal fluorescence investigation of the pharmacokinetics of liposomal BPD-MA drug delivery in a Lewis lung tumor on a mouse. The BPD-MA is fully within the microvasculature immediately after the intraveous injection (left, at 0 mins), but later localizes in the endothelium, and two hours later leaks out into the surrounding tumor tissue (right, at 120 mins). Imaging parameters: 2.5X, 0.07 NA dry objective lens, pinhole diameter 5-15 resels (v = 8-25 optical units, with measured sectioning 300 μm-1mm), excitation wavelengths 458-528 nm (Argon-ion multilines), detection through 560 nm long-pass filter, averaging 2-4 video-rate frames, illumination power 10-20 milliwatts on the skin surface, depth ~100 μm, dosage 4 mg/kg injected intravenously.